ORIGINAL RESEARCH ARTICLE

Carbonitride Strengthening of $Mo_5Nb_{35}Ti_{30}V_{30}$ Refractory High-Entropy Alloy Manufactured by Laser Powder Bed Fusion

LUCY FARQUHAR, ELAINE LIVERA, ROBERT SNELL, JONAH SHRIVE, LUKE JONES, HASSAN GHADBEIGI, IAIN TODD, and RUSSELL GOODALL

Previous research into refractory high-entropy alloys (RHEAs) often focused on optimizing alloys with solid solution phases by adjusting elemental compositions and refining microstructure. To be suitable for critical structural applications, formation of secondary phases, such as those seen in the microstructures of many superalloys, is an area which is still in the early stages of exploration for RHEAs. In this work, a new $Mo_5Nb_{35}Ti_{30}V_{30}$ RHEA is manufactured *via* laser powder bed fusion and subsequently heat treated, inducing the formation of a TiCN phase, initially on cell and grain boundaries (GBs) after 1 hour. After prolonged 24-hour heat treatment the TiCN on the GBs coarsens and the cellular substructure is removed. Samples are then compression tested, all showing ductile failure. Due to the strengthening caused by interstitial elements in the body-centered cubic (BCC) matrix phase, recovery of the cellular substructures and micron-scale TiCN on GBs, the 24-hour heat-treated samples showed increased compressive strength and ductility compared to the as-built samples. TiCN largely grows at a 45 deg misorientation angle about the [100] axis in the BCC matrix phase, hence Kernel average misorientation (KAM) maps show dislocation pile up at the phase boundaries and at the high angle grain boundaries in the recovered microstructure. Susceptibility of RHEAs to atmospheric interstitial infiltration is a concern in the RHEA field; however, this work shows that, if controlled, exposure to these elements can result in beneficial dual-phase microstructures, interstitial strengthening and improved material properties as a result.

https://doi.org/10.1007/s11661-025-07731-6

I. INTRODUCTION

HIGH-ENTROPY alloys (HEAs) were first proposed in 2004 and are known for their microstructural stability and retained mechanical properties at elevated or cryogenic temperatures.[1,2] They were first defined as containing 5 to 13 elements at 5 to 35 at. pct; however, this definition has since expanded to include differing numbers of elements and compositional variations outside this range. The first refractory HEAs (RHEAs) were proposed in 2010 and have been explored for their potential, in particular for high-temperature applications.[3] However, RHEAs are especially difficult to manufacture by conventional methods due to the high melting points of the elements concerned and their susceptibility to oxidation.[4] Vacuum arc melting has previously been the preferred route to manufacture these materials,[5–8] but more recently additive manufacturing (AM) has gained popularity as a method by which to produce homogeneous RHEAs.[9–11] AM also offers the advantage of being able to create near-net shape components, reducing the amount of machining required and providing a benefit as refractory metals typically are difficult to machine by conventional machining methods.[12]

In AM, parts are built up layer by layer allowing geometries that are not manufacturable by traditional means and reduced material wastage. Laser powder bed fusion (PBF-LB/M) is a type of AM process where parts are built by sequentially melting layers of powder deposited in a powder bed using thermal energy supplied by a focused high-powered laser beam. Few RHEAs have been manufactured using this method and where they have, it is often through the use of blended elemental powders due to the cost and difficulty

LUCY FARQUHAR, ELAINE LIVERA, ROBERT SNELL, JONAH SHRIVE, IAIN TODD, and RUSSELL GOODALL are with the Department of Materials Science and Engineering, University of Sheffield, Mappin Street, Sheffield, S1 3JD, UK. Contact e-mail: laufarquhar1@sheffield.ac.uk LUKE JONES and HASSAN GHADBEIGI are with the Department of Mechanical Engineering, University of Sheffield, Mappin Street, Sheffield, S1 3JD, UK. Contact e-mail: r.goodall@sheffield.ac.uk
Manuscript submitted August 22, 2024; accepted February 16, 2025.

Published online: 09 March 2025

associated with manufacture of bespoke RHEA powder.[13–17] Very few publications have therefore manufactured RHEAs *via* PBF-LB/M with pre-alloyed powders, with only a few using optimized spherical powders.[18–20]

Generally, HEAs were initially appealing as a research area due to the expectation of their tendency to form single solid solution phases, stabilized by high mixing entropy. But more recently, efforts have been made to initiate the formation of beneficial precipitates and secondary phases in RHEAs, such as carbides and nitrides, to increase strength, while maintaining the ductility afforded by a solid solution phase.[21–28] However, using AM in isolation or even along with post-process heat treatment to produce carbide or nitride secondary phases in RHEAs is still not common practice.[29–31]

In this work, a $Mo_5Nb_{35}Ti_{30}V_{30}$ RHEA is manufactured *via* PBF-LB/M. This composition was developed by Farquhar *et al.* for use in in PBF-LB/M due to its printability and single phase body-centered cubic (BCC) microstructure.[32] The resulting manufactured samples are then subjected to heat treatment, to reduce residual stress and to recrystallize cellular substructures but also to promote the formation and growth of a secondary carbonitride phase TiCN, caused by atmospheric infiltration. These samples, along with samples in the as-built condition are compression tested to assess the effect of the precipitated TiCN phase and interstitial elements on strength and ductility. The work reported here illustrates that although infiltration of atmospheric impurities is often detrimental to material properties, the controlled exposure to small amounts of interstitials and secondary phase formers during heat treatment can result in enhanced mechanical performance of RHEAs.

II. MATERIALS AND METHODS

The powder feedstock in this work was produced by multiple melting in a cold copper crucible, followed by crushing and radio-frequency plasma spheroidization by Metal Powder Emergence, UK. The powder was sieved through a 52 μm sieve prior to use. All specimens were manufactured using the reduced build volume adaptation on an Aconity3D Mini PBF-LB/M machine, with a laser spot size, focused on the powder bed, of 70 μm and a maximum laser power of 190 W. The PBF-LB/M process was completed in an inert argon atmosphere, where oxygen infiltration was limited to 100 ppm. 8 mm $\times$ 8 mm cylindrical samples were manufactured on a 55-mm diameter Ti–6V–4Al substrate for compression and microstructural analysis. Prior to this work an iterative statistical design of experiment was completed in order to obtain optimal PBF-LB/M parameters to ensure nominally dense parts. The resulting parameters which are used in this work are: laser scanning velocity 600 mm/s, hatch spacing of 17 μm, power 190 W, layer height of 30 μm, and a hatch rotation angle of 67 deg. After removal from the substrate, five samples were left in the as-built (AB) condition while others were heat treated. Heat treatments were completed in an inert furnace with a flow of 99.998 pct purity argon gas (Pureshield Argon supplied by BOC) and a Ti getter. Samples were inserted into a pre-heated furnace and then furnace cooled. Five samples received a 1-hour heat treatment (1HT) at 1200 °C to reduce residual stress and five other samples were heat treated for 24 hours (24HT) at 1200 °C to attempt re-crystallization and possible secondary phase precipitation. Quasi-static compression testing on the samples was completed using a 250-kN capacity Schenck servo-hydraulic Universal Test Machine, with a fixed crosshead displacement rate such that a strain rate of 0.001 s^{-1} was achieved in the elastic region. Four samples of each type were compressed parallel to the build direction. Samples were placed centrally in custom manufactured compression platens with a diameter of 50 mm and a surface hardness greater than 400 HV. The platens were lubricated with machine oil to reduce barrelling and the test was stopped when the load exceeded 200 kN. Compression curves were also compliance corrected. For microstructural characterization, all samples, including those compression tested, were sectioned parallel to the compression/build direction and were prepared using standard material grinding and polishing methods.

The particle size distribution (PSD) for the powder was analyzed using a laser diffraction particle size analyser (Mastersizer 2000, Malvern, UK). Inductively coupled plasma optical emission spectroscopy (ICP-OES) was used to assess metallic element content of the powder, AB, and heat-treated samples. O and N content was found using thermoconductivity and infrared (IR) absorption (Eltra ONH 2000 Analyser) and the C content was obtained using combustion/IR analysis. All bulk elemental analysis was done by Sheffield Assays, UK following the ATM167, ATM149, and ATM82 standards. Phase characterization was performed by X-ray diffraction (XRD) on a Bruker D2 Phaser Diffractomer using a Cu K_α ($\lambda = 1.54$ Å) radiation source. Scanning electron microscopy (SEM) was carried out on the AB and heat-treated samples before compression, using a FEI Inspect F50 SEM. Analysis was completed with a working distance of approximately 10 mm, where the accelerating voltage and spot size were 20 kV and 3.5, respectively. Electron backscattered diffraction (EBSD) and energy dispersive X-ray spectroscopy (EDS) was conducted using a JEOL 7900F field emission gun (FEG)-SEM, equipped with an Oxford Instrument's symmetry detector. An accelerating voltage of 20 kV was used, along with a step size of 0.4 μm, to characterize texture and a step size of 0.018 μm to study precipitate formation. Grain reconstruction was performed using MTEX software with low and high angle grain boundary (HAGB) thresholds of 3 and 10 deg, respectively.[33] Inverse pole figure (IPF) maps, pole figures, and kernel average misorientation (KAM) maps were produced from the reconstructed data. Identification of the TiCN secondary phase was done through combined use of EDS to identify the constituent elements and the XRD pattern with peak positions identifying a superposition of the TiC and TiN peaks. For EBSD phase identification, the phase symmetry for TiC was used due to the similarity in lattice

parameters (4.33 Å (TiC) and 4.24 Å (TiN)). The confidence interval used for phase identification was 3, corresponding to the 3-sigma confidence interval for a normal statistical error distribution.

III. RESULTS AND DISCUSSION

A. *Powder Analysis*

As can be seen in Figure 1, the powder is largely spherical; however, some smaller clusters of satellite particles are present. These smaller particles are reflected in the PSD, which also indicate the presence of particles above 52 μm, despite being sieved prior to use. The percentile D_{10}, D_{50} and D_{90} values for the PSD, are 11.9, 28.0, and 57.3 μm, respectively. The larger particles are most likely caused by agglomerates of the finer particles, or by elliptical particles that are able to pass through the sieve. These particles likely have two dimensions below the mesh size due to incomplete spherodization in the powder production process. Nb and Mo rich particles, which deviate from the nominal composition, are also present in the powder. In some particles, the Nb and Mo content reaches up to 75 and 10 at. pct, respectively, with Ti and V compositions remaining constant throughout the powder. There is also the appearance of some powder particles containing Ta contamination.

B. *Bulk Elemental Analysis*

ICP-OES results for the powder and all bulk samples are shown in Table I. The values of measured composition for the constituent elements are all within 2 wt pct of the nominal composition with Nb showing the greatest deviation. There is a high level of O, N, and C reported, which could cause the formation of pores, balling, cracking or microstructural variability that would not otherwise be present without these interstitial elements.[34–36] RHEA powders such as this are difficult to manufacture due to the high temperatures needed for melting as well as their tendency to oxidize. Therefore, it is likely that the crushing and spherodization manufacturing route introduced more O into the powder than other routes, such as electrode induction gas

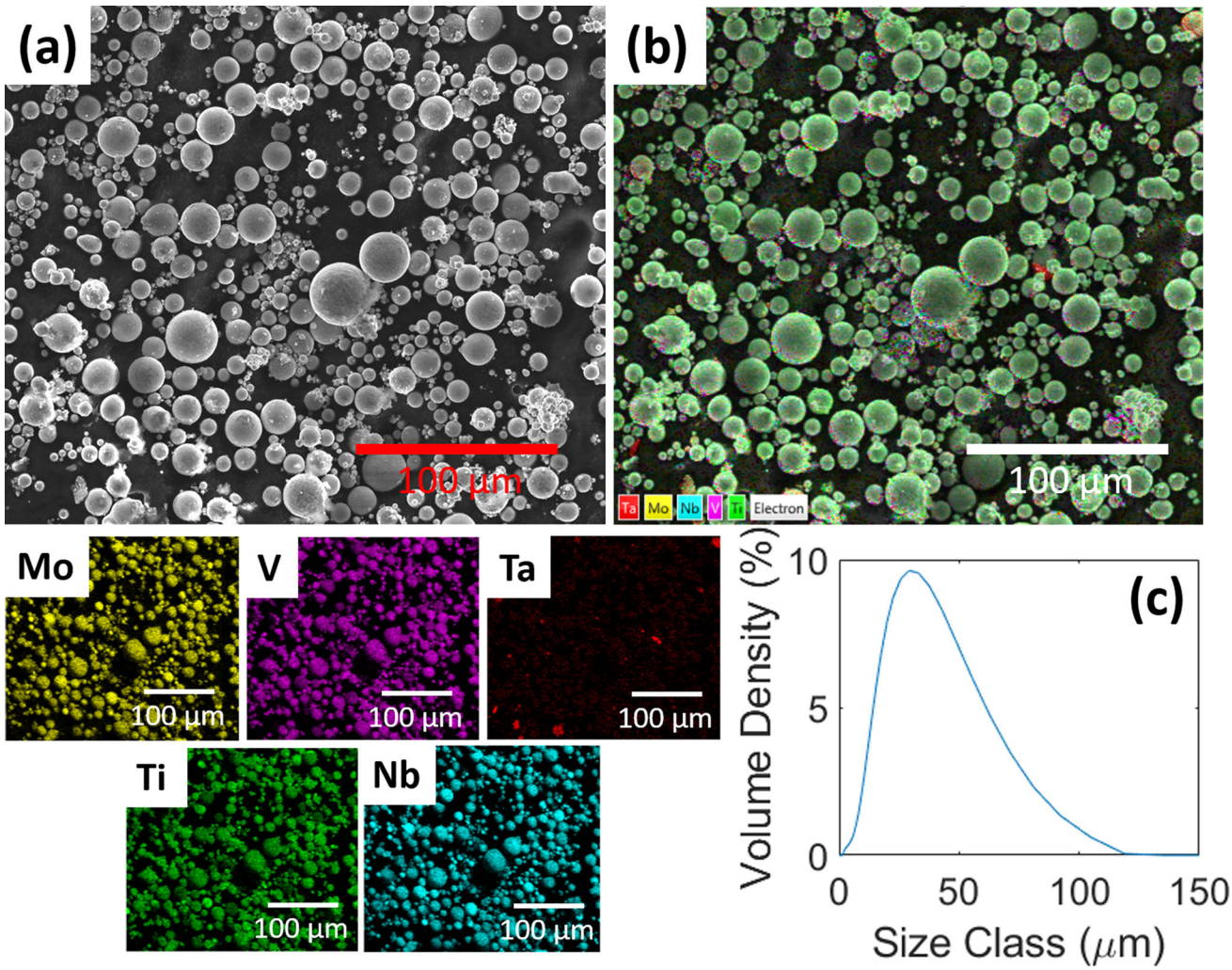

Fig. 1—(*a*) Backscattered electron (BSE) image showing the powder feedstock used. (*b*) Overlaid EDS map showing the elemental distributions, along with maps for each element in the nominal composition as well as the contaminating Ta. (*c*) PSD for the powder.

atomisation (EIGA), would have.[37] However, this apparent contamination of O, and particularly N, in the powder could also be due to prolonged storage of the powder under air before ICP-OES was conducted (a period of 9 months of storage after manufacture), therefore not giving an accurate representation of the O and N content of the powder immediately prior to manufacture of samples.

The powder, and therefore also the corresponding bulk samples, also contain approximately 0.3-wt pct Ta contamination, as was also seen in the EDS maps in Figure 1, showing interspersed Ta-rich powder particles. As this was found in the powder when analyzed before any processing, it is assumed this was introduced in the manufacturing process, likely as the powder supplier also manufactures Ta-containing alloy powders using the same process. After PBF-LB/M, the AB sample shows a small increase in O, N, and C content, which is typical after an AM process.[34] The O content also increases with increasing heat treatment time, due to atmospheric infiltration, or possibly residual oxygen in the Argon gas. This is also indicated by the layer of apparent oxidation which formed on the sample surfaces after both heat treatment times. According to these results, both the C and N increase after 1HT, and then reduce after 24HT, which is unexpected, as further results in this work indicate an increase in these elements, due to the precipitation and coarsening of the TiCN phase. This lack of substantial increase in the N and C composition may indicate that there is limited pick up of these elements during heat treatment and that interstitial N and C introduced in powder manufacture is merely diffusing and precipitating on grain boundaries instead of remaining interstitial in the BCC matrix. However, there are many other potential reasons for the lack of increase in the composition of these elements, such as a change in the composition of the heat treatment atmosphere (which was not continuously monitored in the process) between the two heat treatments; therefore, the discrepancy between these results is likely within the margin of error for detection of these elements.

C. *Microstructure*

Figure 2 shows EBSD maps and pole figures for the AB, 1HT, and 24HT samples. The AB sample shows epitaxial columnar grain growth, typical of AM processes, resulting in a texture in the ⟨100⟩ direction, which here aligns with the build direction in these images. The texture of the samples reduces with heat treatment time; however, it has not been completely removed and a ⟨100⟩ texture still remains in in the 24HT sample.

As well as partial re-crystallization, XRD scan results, shown in Figure 3, indicate that all samples have a main BCC phase with a lattice parameter between 3.210 and 3.224 Å. The peak corresponding to the (200) plane in the AB sample has a lower peak intensity due to sample orientation in the XRD scan, as the EBSD does not indicate a change in grain orientation substantial enough to cause this reduction. The samples show the appearance of small peaks at 35.6 and 42.4 deg after heat treatment, corresponding to the onset of formation of a secondary phase. The EBSD phase maps and EDS results for the 24HT sample are shown in Figure 4, where the secondary phase has formed on the GBs of the BCC matrix grains. This secondary phase has been identified as a solid solution of both TiC and TiN which both have very similar peak positions and are both face-centered cubic (FCC) structures, otherwise known as TiC_xN_{1-x}, here referred to as TiCN. Phase maps for the 1HT and 24HT samples in Figure 4, confirm the formation of this FCC TiCN phase. The exact level of C and N content in this phase was unable to be resolved with EDS, as the precipitates are less than 1 μm in size, however broadly speaking the Ti content stays consistently between 26 and 30 at. pct, while C and N remain elevated above the content in the surrounding phase.

Figure 5 shows the secondary phase precipitation and growth after differing heat treatment times. The AB sample shows the formation of dislocation cells within grains, the size and shape of which correspond with the position in the melt pool. But no precipitation of a secondary phase. After heat treatment for 1 hour, the secondary phase has begun to precipitate on the GBs and partially on the cell boundaries (CBs), which have not yet recrystallized, a phenomenon seen previous in heat-treated nickel-based alloy samples made by PBF-LB/M.[38,39] The size of the TiCN precipitates on the CBs varies significantly between 10 and 600 nm in size, following the pattern of cells left by the solidification of successive melt pools and are finely dispersed with a needle-like shape on the CBs. The TiCN present on GBs is clustered and interconnected, with sizes from approximately 100 nm to 1 μm as seen in Figure 4.

In the 24HT sample, the dislocation cells have recovered leaving a small number of larger remaining intragranular secondary phase particles. However, the majority of these precipitates have likely dissolved into the matrix phase forming interstitials in the BCC lattice or have diffused to GBs; EDS was however unable to resolve the change in C content. Due to the diffusion to GBs and possible infiltration of further N and C, the secondary phase has coarsened and is now most often present on GBs, and the size of the TiCN particles is now approximately between 1 and 4 μm in length.

An example of the TiCN precipitates in the 24HT sample and the corresponding GB misorientation map is shown in Figure 6. In the misorientation histogram, there is a high-intensity peak at 45 deg showing the prevalence of this angle of misorientation between grains. Considering the misorientation map, this angle likely corresponds to the growth of the TiCN secondary phase at 45 deg misorientated about the [100] axis of the BCC phase. Consideration of atomic structures between these two phases, shown in Figure 6 gives evidence of a structural correspondence at this angle, first reported by Bain *et al*. in martensitic steels[40] and further outlined in the review by Grimvall *et al*.[41] In the schematic shown in Figure 6(d), the FCC phase grows from the {110} plane in the BCC matrix phase, to become the {100} plane in the FCC phase. For this to achieve a 45 deg misorientation about the [100] axis with correspondence of the atomic sites with a BCC phase of given lattice parameter a, the lattice parameter of the FCC phase must be approximately equivalent to $a\sqrt{2}$. Here, the lattice parameter of the BCC phase is approximately

Table I. Elemental Composition of the Powder Feedstock, AB, 1HT, and 24HT Samples, Compared with the Nominal Composition, including Entrained O, N, and C

Element (Wt Pct)	Mo	Nb	Ti	V	Ta	O	N	C
Nominal	7.16	48.6	21.4	22.8	—	—	—	—
Powder	7.47	50.2	20.8	21.3	0.31	0.073	0.091	0.086
AB	7.56	50.6	20.4	21.1	0.35	0.13	0.13	0.097
1HT	7.65	51.0	19.9	20.8	0.32	0.27	0.23	0.093
24HT	7.64	51.3	19.7	20.6	0.34	0.45	0.18	0.083

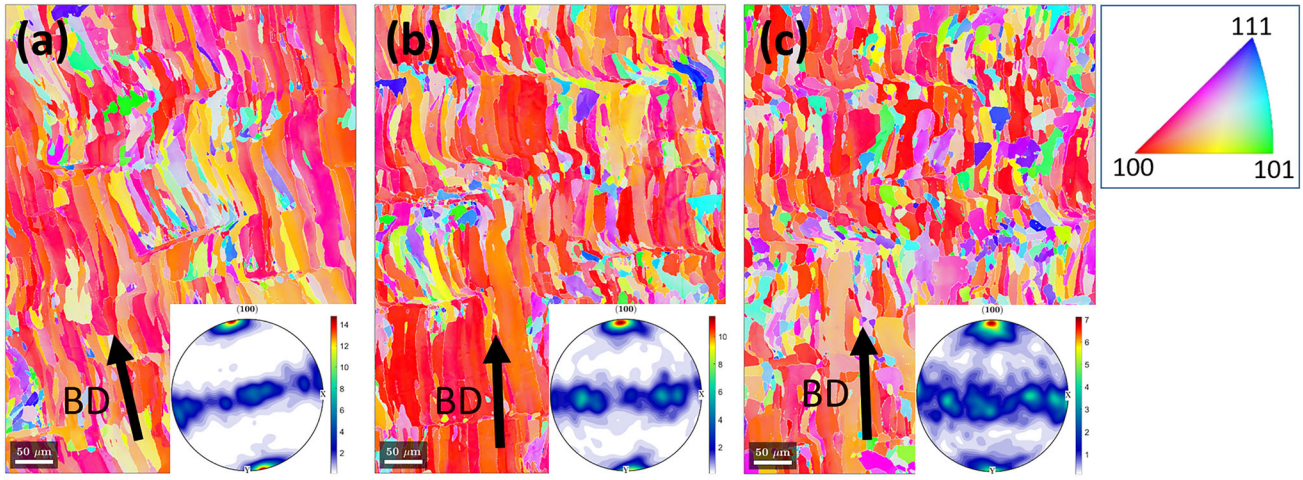

Fig. 2—EBSD inverse pole figure (IPF-Y) images and corresponding (100) pole figures for the (*a*) as-built, (*b*) 1HT, and (*c*) 24HT, showing microstructural texture and the onset of grain crystallization. BD here stands for build direction from the PBF-LB/M process.

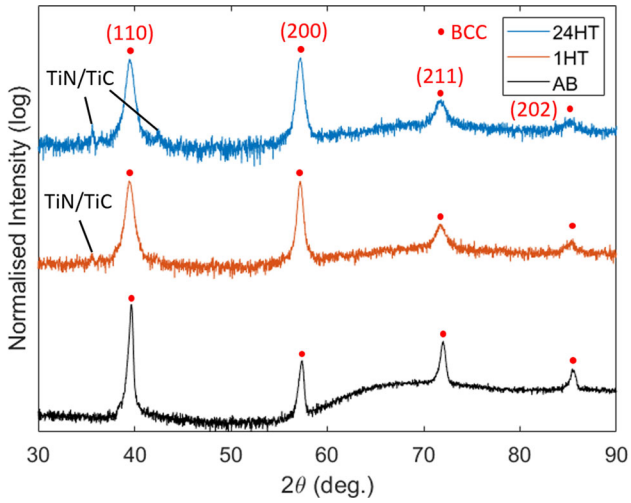

Fig. 3—XRD patterns of the AB, 1HT, and 24HT samples, showing the onset of the formation of TiCN.

3.22 Å so $a\sqrt{2} = 4.55$ Å. The lattice parameter of the TiCN phase in this case is between $a_{FCC} = 4.24$ Å (TiN) or $a_{FCC} = 4.33$ Å (TiC). It can therefore be suggested that the growth of TiCN tends to nucleate on GBs of BCC grains and grows into a neighboring grain, resulting in 45 deg GB on one edge of an elongated FCC grain. Alternatively, where diffusion to the GB has not occurred after the annealing of the cellular microstructure, TiCN has formed with a 45 deg total misorientation about the [100] axis from the surrounding BCC grain.

D. *Mechanical Behavior Under Compression*

Representative engineering stress *vs* engineering strain curves and the corresponding yield strength values for the AB, 1HT, and 24HT samples are illustrated in Figure 7. The raw compression curves are also shown in Appendix A. All samples exhibited ductile failure and all reached the imposed force limit of the compression test equipment used at 200 kN, with the heat-treated samples showing some spallation of surface oxides at higher strains. The AB sample has a high mean yield strength of 1101 MPa, due to the hierarchical microstructure present, including melt pools, columnar grains, cellular sub-structures, and high dislocation density, all of which impede dislocation motion.[42] However, as many of these structures are still present in the other samples, it is thought that the high strength is also influenced by the residual stress commonly induced during AM. Due to the AM processing, high tensile stresses are induced at the edges of the part and compressive stresses are induced at the center.[43–45] Therefore the high initial residual tensile stresses within the parts may be resulting in an apparent increase in the compressive strength.[46]

The 1HT sample has a texture much the same as the AB sample and retains the cellular sub-structures, along with the onset of precipitation on GBs and CBs. In

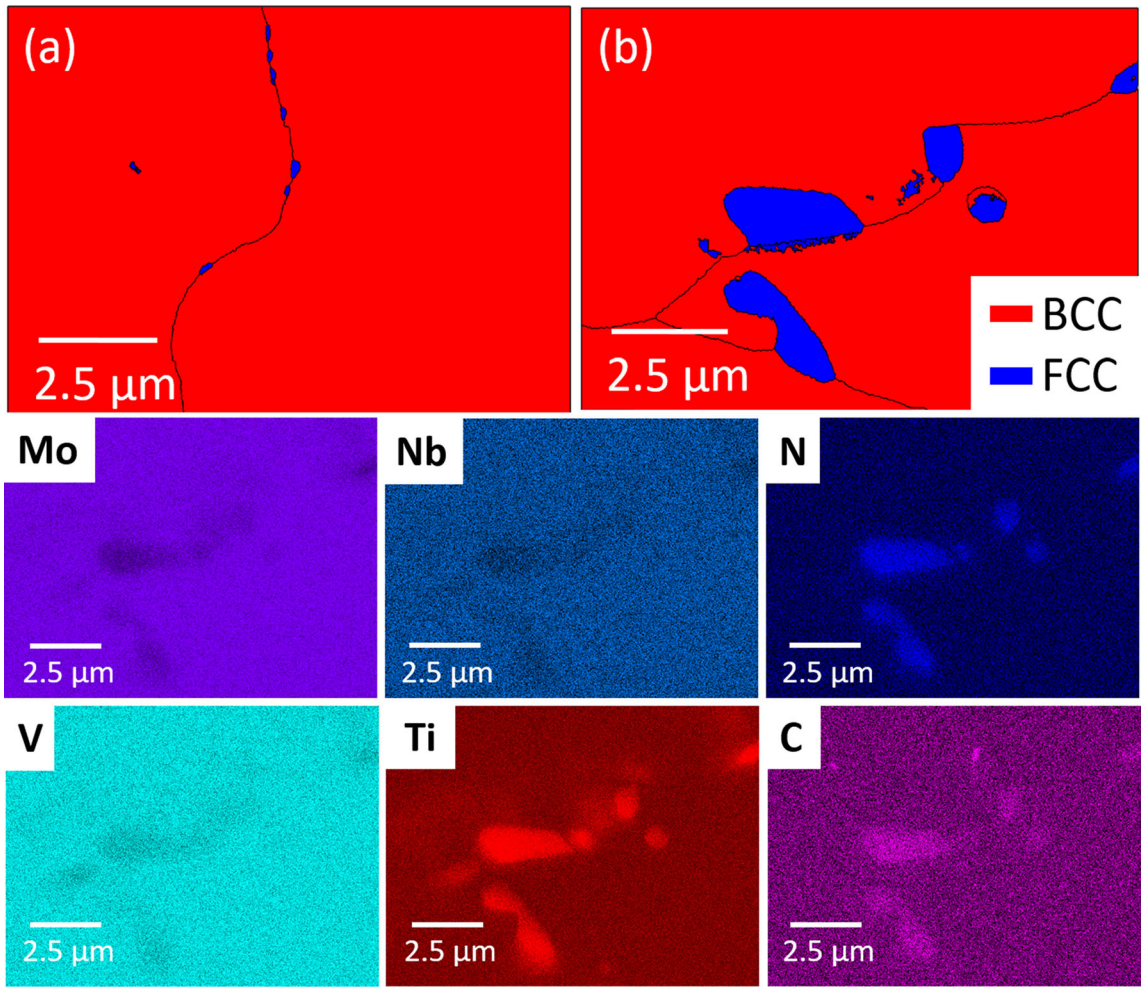

Fig. 4—(*a*) Phase map of the 1HT, showing the start of the formation of FCC TiCN. (*b*) Phase map of the coarsened GB TiCN phase in the 24HT sample, along with EDS maps showing the distribution of elements in the nominal composition, as well as N and C in the TiCN phase.

theory this alone should result in an increased strength, due to secondary phase strengthening and increased GB misorientation. However the mean yield strength of this sample is 903 MPa, a reduction compared to the AB sample. This is likely due to the reduction in residual stresses which can result from even a short heat treatment.[47] The slight reduction in texture could also be a contributing factor to the reduction in yield strength, as well as possible partial recovery. The initial hardening rate of this sample is similar to that of the AB sample, indicating that these samples are plastically deforming *via* the same dislocation slip mechanisms and that the dispersoid nanoprecipitate particles are having very little effect on creating dislocation pile up. However, due to the reduced yield stress the total strain of the sample at 200 kN is comparable to that achieved by the 24HT sample.

In the 24HT sample, the cellular substructure has been completely removed and the secondary TiCN phase has coarsened and resides mostly on GBs. This sample has a vastly reduced dislocation density, due to the recovery of the cellular structures, compared to the other sample conditions, leading to an increase in ductility and reduction in initial hardening rate. Alongside this, the increase in TiCN concentration indicated by XRD, as well as the infiltration of interstitial contaminants, such as O, C and N, has meant that the material also has an increased compressive yield strength of 1148 MPa, when compared to the 1HT sample. It is thought that the increased presence of these elements interstitial in the BCC lattice is the main cause of this improved compressive strength. Even though more generally, it is reported that interstitial infiltration of these elements and the formation of their compounds results in embrittlement as well as increased strength.[48] This result shows that, at low concentrations, atmospheric infiltration can provide enhancement to mechanical properties of RHEAs, without compromising ductility, especially when paired with heat treatment of a hierarchical AM microstructure.

E. *Deformed Microstructure*

EBSD and kernel average misorientation (KAM) maps for the AB, 1HT, and 24HT samples are shown in Figure 8. Each of the 3 samples show shearing of the grains present at 45 deg, consistent with the angle of maximum shear stress in uniaxial compression. The AB sample displays the CBs indicated by the oval structures

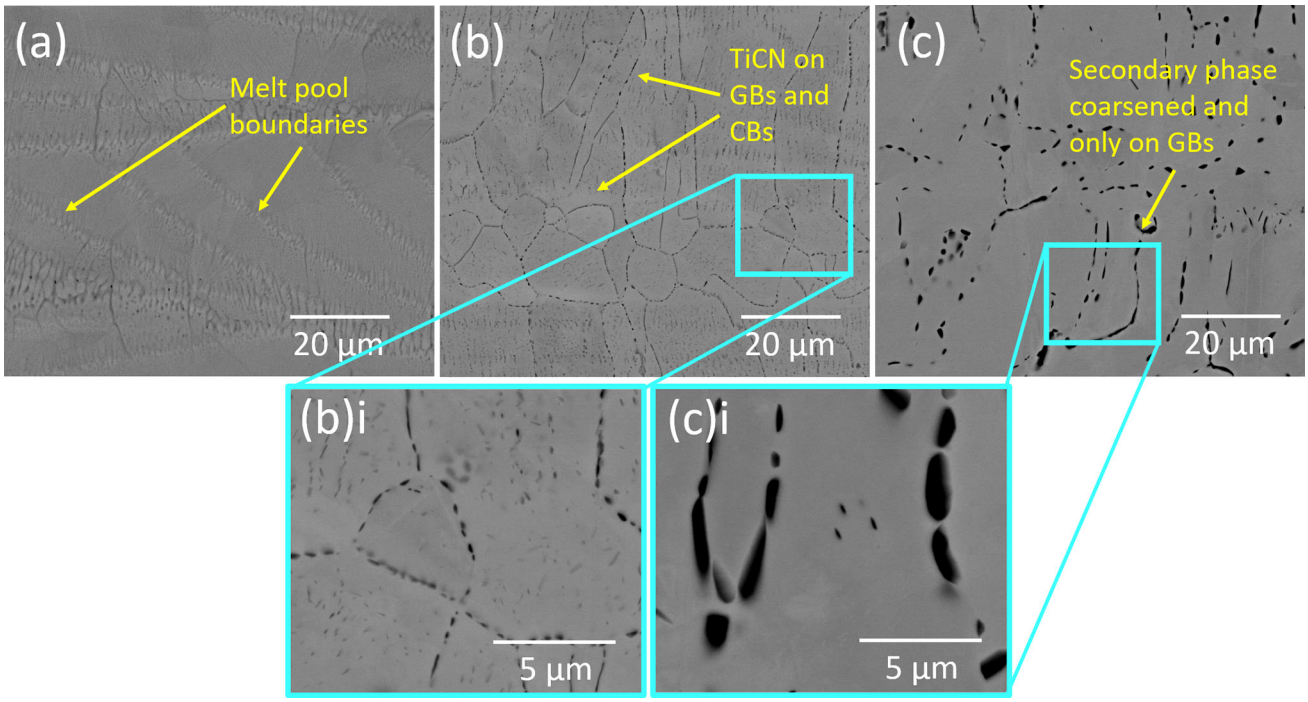

Fig. 5—BSE images of the (*a*) AB, (*b*) 1HT and (*c*) 24HT samples showing the formation and evolution of the TiCN secondary phase and the recovery of the cellular microstructure. *(b)i* and *(c)i* Show high-magnification BSE images of the shape and size of TiCN precipitation in the 1HT and 24HT samples, respectively.

within grains with higher KAM values. The high level of misorientation and therefore dislocations still distributed throughout this sample, due to the cells, explains the high strength and reduced ductility shown in the compression curve as the motion of dislocations is impeded. The level of non-indexed areas and KAM at GBs in the AB sample is also reduced compared to the heat-treated samples, indicating there is less dislocation build-up in those areas.

The 1HT sample has a much higher average KAM and much more non-indexed areas compared to the other samples. There is also a slight development from the oval shaped cell morphology seen in the KAM for the AB sample, although this could be attributed to the grains which are imaged. Due to the relief of residual stress to reduce the yield strength, for the same maximum load, there is an increase in plastic deformation consistent with the compression curve, ending in a strain of 63 pct compared to 55 pct for the AB sample. The fine nano-TiCN secondary phase precipitates also create HAGBs and dispersoid barriers within grains which likely increases the number of isolated dislocation pile ups, reflected by the non-indexed pixels in this sample. Therefore there are no micro-scale dislocation pile ups which traverse a whole grain on the same plane as there are in the 24HT sample. However despite the strengthening effect commonly associated with these types of dispersoid precipitates and slight interstitial infiltration, the effect of reduced residual stress has had a larger influence causing a reduced yield strength.

In the 24HT samples, there are bands of increased misorientation and therefore increased slip across grains which were previously recovered, removing the cellular structures. These bands correspond to the ⟨111⟩ direction, the predominant slip direction in BCC materials.[49] This explains why there extensive 45 deg slip bands in grains 1 and 2, but little deformation in grain 3, as the critical resolved shear stress for 1 and 2 is higher for those grains which are more aligned with the ⟨111⟩ direction. The enhanced ductility of this sample is thought to be due to the unimpeded dislocation motion within the recrystallized grains, which would also explain why the highest KAM contrast is found interconnected to the GBs. After slip within the grains, dislocation pile up (indicated by the higher misorientation) is due to either the coarse TiCN secondary phase particles, or HAGBs, which are more predominant in a sample which is partially recrystallized compared to the AB sample. It is expected that the precipitation of the TiCN on CBs in the 1HT samples, for example, causes a barrier to dislocation slip through the distribution of dispersoid particles. However, elements interstitial in the BCC matrix seem to have a much stronger comparative effect on the compressive yield strength. This confirms that substantial strengthening does indeed come from the increased TiCN content, but the interstitial elements in the solid solution of the BCC lattice increases compressive strength more substantially, and the corresponding ductility can be increased in tandem through recovery of the cellular structures.

IV. CONCLUSION

In this work, the new $Mo_5Nb_{35}Ti_{30}V_{30}$ RHEA was manufactured *via* PBF-LB/M and subsequently heat treated. A secondary phase precipitated after heat treatment, most likely due to diffusion of contamina

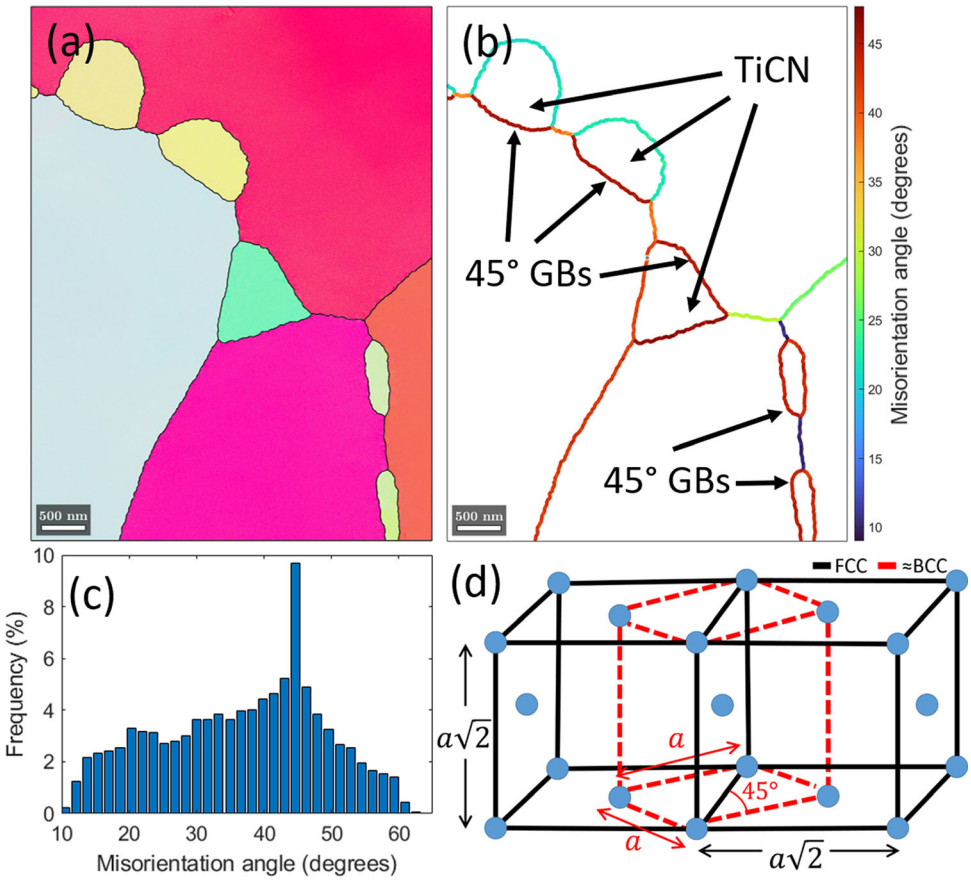

Fig. 6—(*a*) EBSD IPF-Y map of the 24HT sample and the GB TiCN secondary phase present. (*b*) Map of HAGB misorientations in the 24HT sample. (*c*) Misorientation histogram for all HAGBs above 10 deg in the EBSD image of the 24HT sample shown in Fig. 2. The peak at 45 deg corresponds to the TiCN secondary phase growth direction at 45 deg about the [100] axis of the BCC matrix phase. (*d*) Schematic of the growth mechanism of the FCC TiCN phase from the BCC matrix phase.

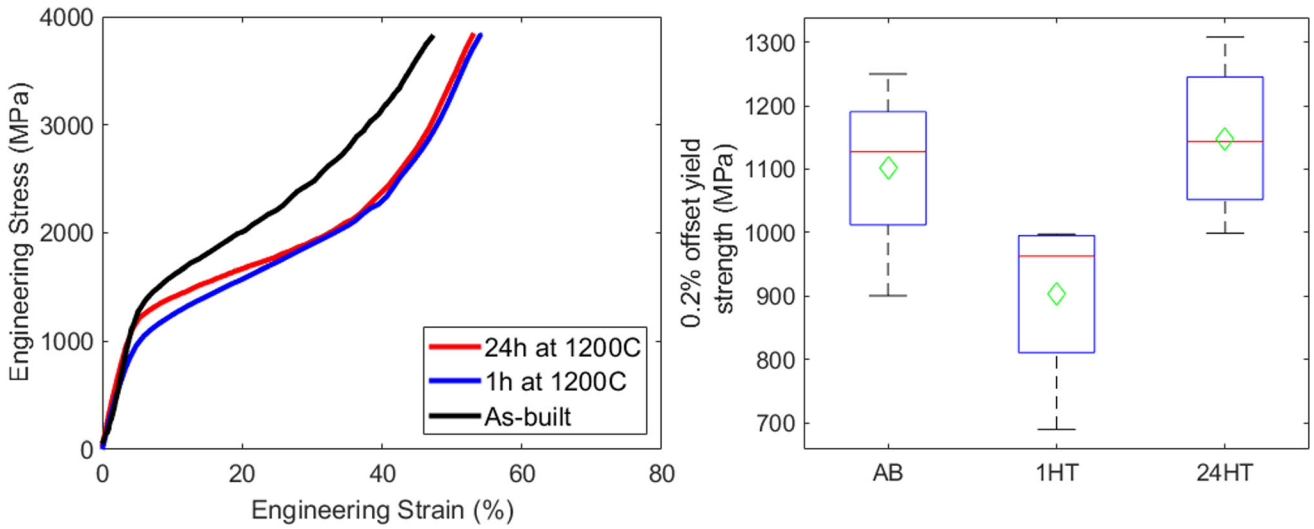

Fig. 7—Example engineering stress *vs* engineering strain curves for compression of the AB, 1HT, and 24HT samples and boxplots for the 0.2 pct offset compressive yield stress for each sample type. Median values are shown with a red line and mean values are shown by a green diamond (Color figure online).

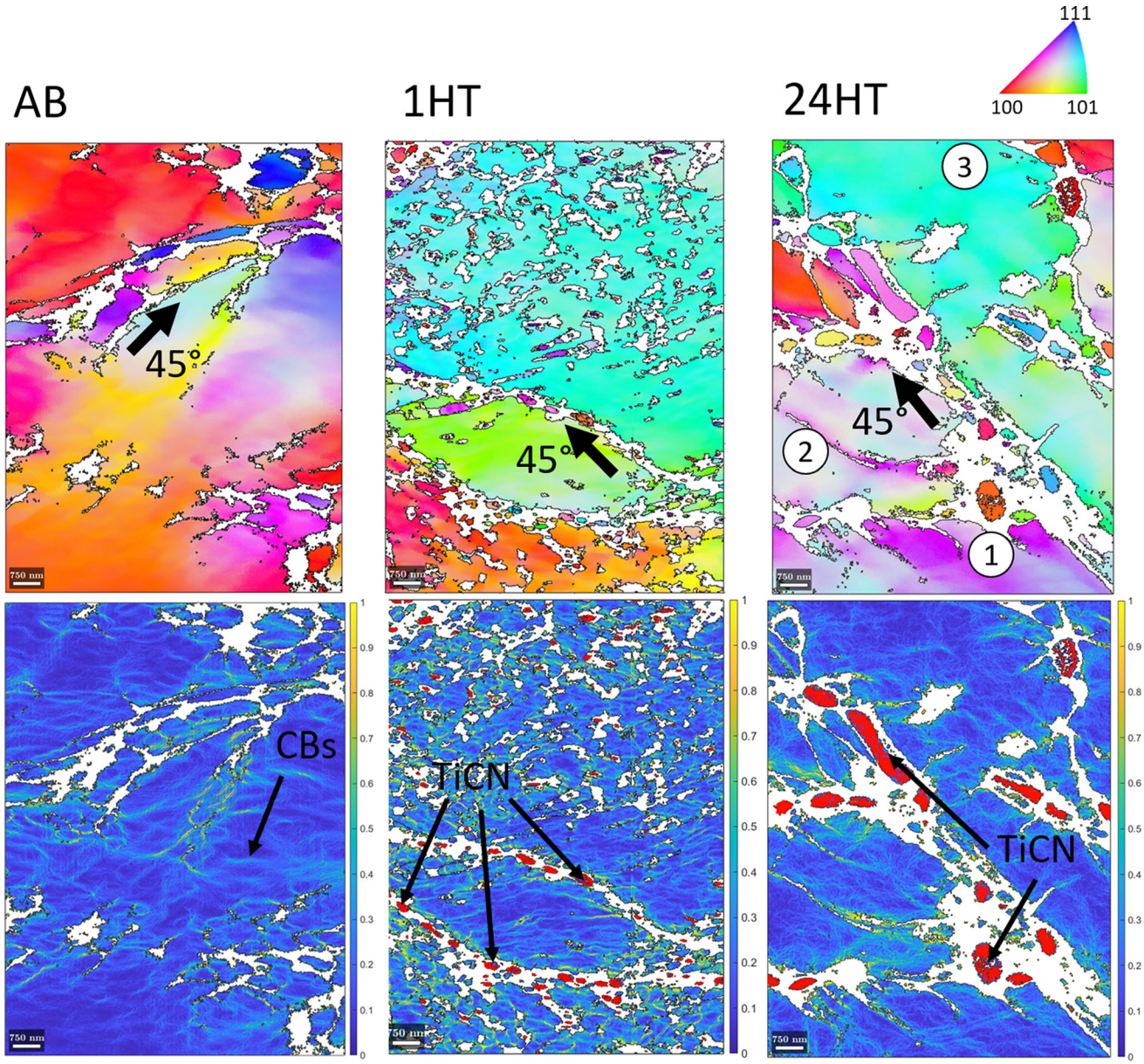

Fig. 8—EBSD IPF-Y images and KAM maps showing the deformed microstructures of the AB, 1HT, and 24HT samples. The white areas represent non-indexed pixels, due to extensive misorientation, caused by the compressive deformation, within the step size used. In the KAM maps, TiCN is shown in red. The vertical direction in these images corresponds to both the build direction and the compression direction. The colorbar for the KAM maps represents the KAM angle in degrees and the shear slip angle of 45 deg is also indicated (Color figure online).

and the partial infiltration of N and C, creating fine precipitates after 1 hour and coarse GB precipitates after 24 hours at 1200 deg. The corresponding samples were compression tested and the results analyzed along with the deformed microstructure. The key findings are summarized as follows:

- Pre-alloyed powder was used to manufacture samples which were then heat treated to reduce residual stress, recover the cellular microstructure, achieve a reduction in texture, and precipitate secondary phases.
- Infiltration of atmospheric impurities during heat treatment and diffusion of interstitial elements introduced during manufacture were likely the leading causes for the precipitation of a TiCN secondary phase. This TiCN phase contains varying C and N contents, as confirmed by XRD, EBSD phase analysis, and bulk elemental analysis. The level of O in the samples also increased after printing and with increasing heat treatment duration.
- A fine TiCN phase precipitated on the CBs and GBs on the 100 nm scale in the 1HT sample, while in the

24HT sample, after removal of the sub-structures, the TiCN diffused, increased in concentration, and coarsened on GBs to a micron scale. As well as this, it is also likely that the concentration of C, N, and O interstitial in the BCC matrix also increased with heat treatment time.

- The FCC TiCN preferentially grows at a 45 deg angle about the [100] axis of the BCC phase on GBs, creating a HAGB between the phases.
- Compression testing showed that for the 24HT samples, the probable increase in interstitial elemental content resulted in increased compressive strength, while the ductility increased due to removal of cells and coarsening of the TiCN when compared to the 1HT samples. These results provide an indication toward the relative contributions of dispersoid precipitates and interstitial strengthening in alloys of this kind.
- The infiltration of atmospheric interstitial elements, often thought of as deleterious especially to refractory materials, has here been shown to enhance material strength without compromising ductility when paired with the recovery of the cellular structures formed in PBF-LB/M processing. This combination thereby uses the affinity of RHEAs to react with atmospheric interstitial elements as an advantageous way to strengthen these types of alloys.

ACKNOWLEDGMENTS

This work was supported by Science Foundation Ireland 18/EPSRC-CDT/3584, the Engineering and Physical Sciences Research Council EP/S022635/1 and the Manufacture using Advanced Powder Processes (MAPP) EPSRC Future Manufacturing Hub EP/P006566/1. We wish to acknowledge the Henry Royce Institute for Advanced Materials, funded through EPSRC grants EP/R00661X/1, EP/S019367/1, EP/P02470X/1, and EP/P025285/1, for access to the Aconity3D Mini at The University of Sheffield.

OPEN ACCESS

AUTHOR CONTRIBUTIONS

Lucy Farquhar contributed to conceptualization, methodology, investigation, and writing—original draft. Elaine Livera contributed to investigation, software, and writing—review and editing. Robert Snell contributed to methodology and writing—review and editing. Luke Jones contributed to investigation and writing—review and editing. Hassan Ghadbeigi contributed to Investigation. Iain Todd contributed to supervision and funding acquisition. Russell Goodall contributed to conceptualization, methodology, writing—review and editing, supervision, and funding acquisition.

COMPETING INTERESTS

The authors declare that they have no conflict of interest.

APPENDIX A. COMPRESSION CURVES FOR $MO_5NB_{35}TI_{30}V_{30}$

See Figure 9.

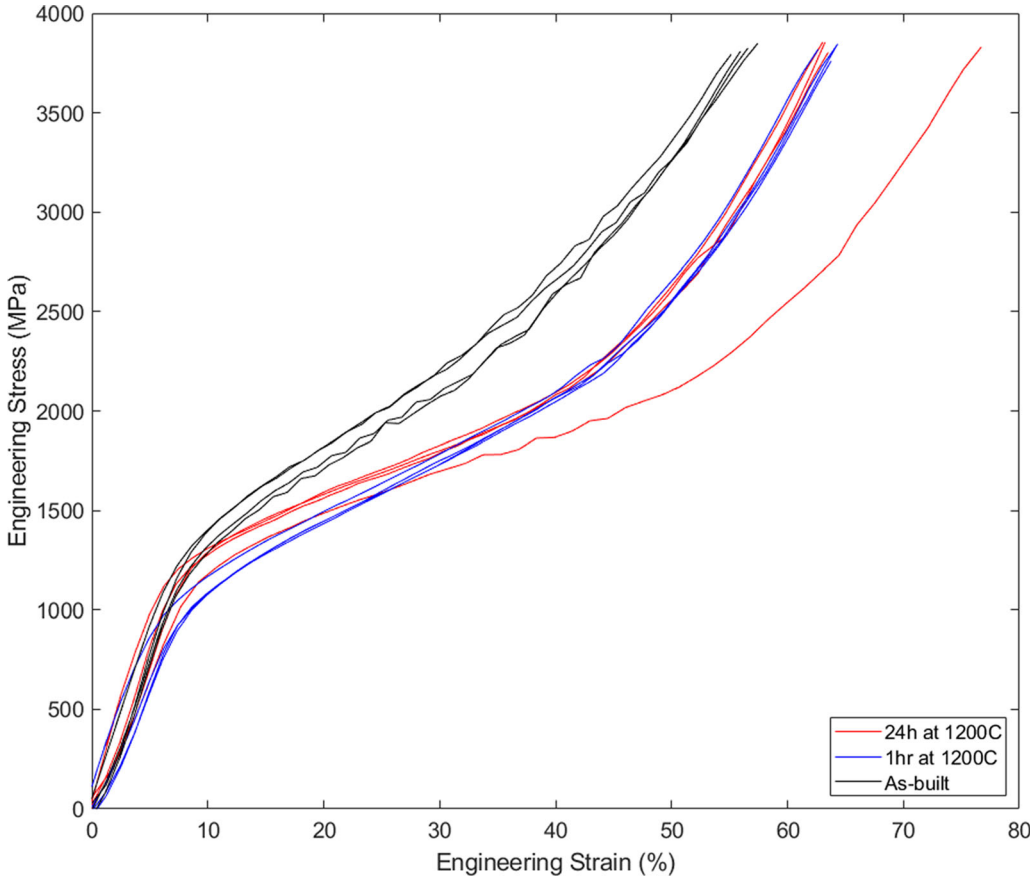

Fig. 9—Compressive engineering stress *vs* engineering strain curves for the $Mo_5Nb_{35}Ti_{30}V_{30}$ RHEA in the as-built and after heat treatment for 1 and 24 h at 1200 °C. These are curves using raw data without correcting for machine compliance.

REFERENCES

1. B. Cantor, I.T.H. Chang, P. Knight, and A.J.B. Vincent: *Mater. Sci. Eng., A*, 2004, vol. 375–377(1–2), pp. 213–18. https://doi.org/10.1016/j.msea.2003.10.257.
2. J.W. Yeh, S.K. Chen, S.J. Lin, J.Y. Gan, T.S. Chin, T.T. Shun, *et al.*: *Adv. Eng. Mater.*, 2004, vol. 6(5), pp. 299–303. https://doi.org/10.1002/adem.200300567.
3. O.N. Senkov, G.B. Wilks, D.B. Miracle, C.P. Chuang, and P.K. Liaw: *Intermetallics*, 2010, vol. 18(9), pp. 1758–65. https://doi.org/10.1016/j.intermet.2010.05.014.
4. J. He, Y. Qiao, R. Wang, Y. Tang, S. Li, X. Liu, *et al.*: *J. Alloys Compd.*, 2022, vol. 1, p. 891. https://doi.org/10.1016/j.jallcom.2021.161963.
5. O.N. Senkov, G.B. Wilks, J.M. Scott, and D.B. Miracle: *Intermetallics*, 2011, vol. 19(5), pp. 698–706. https://doi.org/10.1016/j.intermet.2011.01.004.
6. M.G. Poletti, C.M. McCaughey, G. Fiore, R. Goodall, and L. Battezzati: *Int. J. Refract. Met. Hard Mater.*, 2018, vol. 76(May), pp. 128–33. https://doi.org/10.1016/j.ijrmhm.2018.05.014.
7. L. Lilensten, J.P. CouziniÃ©, L. PerriÃre, J. Bourgon, N. Emery, and I. Guillot: *Mater. Lett.*, 2014, vol. 132, pp. 123–25. https://doi.org/10.1016/j.matlet.2014.06.064.
8. J.P. CouziniÃ©, G. Dirras, L. PerriÃre, T. Chauveau, E. Leroy, Y. Champion, *et al.*: *Mater. Lett.*, 2014, vol. 126, pp. 285–87. https://doi.org/10.1016/j.matlet.2014.04.062.
9. T. Ron, A. Shirizly, and E. Aghion: *Materials*, 2023, vol. 16(6), p. 2454. https://doi.org/10.3390/ma16062454.
10. A. Ostovari Moghaddam, N.A. Shaburova, M.N. Samodurova, A. Abdollahzadeh, and E.A. Trofimov: *J. Mater. Sci. Technol.*, 2021, vol. 77, pp. 131–62. https://doi.org/10.1016/j.jmst.2020.11.029.
11. W. Xiong, A.X.Y. Guo, S. Zhan, C.T. Liu, and S.C. Cao: *J. Mater. Sci. Technol.*, 2023, vol. 142, pp. 196–215. https://doi.org/10.1016/j.jmst.2022.08.046.
12. M. Olsson, V. Akujärvi, J.E. Ståhl, and V. Bushlya: *Int. J. Refract. Met. Hard Mater.*, 2021, vol. 6, p. 97. https://doi.org/10.1016/j.ijrmhm.2021.105520.
13. H. Zhang, W. Xu, Y. Xu, Z. Lu, and D. Li: *Int. J. Adv. Manuf. Technol.*, 2018, vol. 96(1–4), pp. 461–74. https://doi.org/10.1007/s00170-017-1331-9.
14. H. Zhang, Y. Zhao, S. Huang, S. Zhu, F. Wang, and D. Li: *Materials*, 2019. https://doi.org/10.3390/ma12050720.
15. P. Zhu, Y. Yu, C. Zhang, Q. Zhou, B. An, R. Guo, *et al.*: *Int. J. Refract. Met. Hard Mater.*, 2023, vol. 6, p. 113. https://doi.org/10.1016/j.ijrmhm.2023.106220.
16. F. Wang, T. Yuan, R. Li, S. Lin, P. Niu, and V. Cristino: *Int. J. Refract. Met. Hard Mater.*, 2023, vol. 2, p. 111. https://doi.org/10.1016/j.ijrmhm.2023.106107.
17. J. Cai, H. Zhang, L. Wang, X. Sun, X. Xu, X. Guo, *et al.*: *Mater. Sci. Eng. A*, 2023, vol. 10, p. 886. https://doi.org/10.1016/j.msea.2023.145681.
18. C. Liu, K. Zhu, W. Ding, Y. Liu, G. Chen, and X. Qu: *Powder Metall.*, 2022, vol. 65(5), pp. 413–25. https://doi.org/10.1080/00325899.2022.2031718.
19. P. Gu, T. Qi, L. Chen, T. Ge, and X. Ren: *Int. J. Refract. Met. Hard Mater.*, 2022, vol. 6, p. 105. https://doi.org/10.1016/j.ijrmhm.2022.105834.
20. O. Gokcekaya, T. Ishimoto, Y. Nishikawa, Y.S. Kim, A. Matsugaki, R. Ozasa, *et al.*: *Mater. Res. Lett.*, 2023, vol. 11(4), pp. 274–80. https://doi.org/10.1080/21663831.2022.2147406.
21. Y. Wan, Y. Cheng, Y. Chen, Z. Zhang, Y. Liu, and H. Gong, *et al.*: *Engineering*, 2023. https://doi.org/10.1016/j.eng.2023.06.008.
22. Y. Guo, H. Wang, and Q. Liu: *J. Alloys Compd.*, 2020, vol. 9, p. 834. https://doi.org/10.1016/j.jallcom.2020.155147.

23. Y. Tian, W. Zhou, M. Wu, H. Luo, Q. Tan, G. Zhu, *et al.*: *J. Alloys Compd.*, 2022, vol. 9, p. 915. https://doi.org/10.1016/j.jallcom.2022.165324.
24. R. Wang, Y. Tang, Z. Lei, Y. Ai, Z. Tong, S. Li, *et al.*: *Mater. Des.*, 2022, vol. 1, p. 213. https://doi.org/10.1016/j.matdes.2021.110356.
25. J.A. Smeltzer, B.C. Hornbuckle, A.K. Giri, K.A. Darling, M.P. Harmer, H.M. Chan, *et al.*: *Acta Mater.*, 2021, vol. 6, p. 211. https://doi.org/10.1016/j.actamat.2021.116884.
26. S. Wu, D. Qiao, H. Zhang, J. Miao, H. Zhao, J. Wang, *et al.*: *J. Mater. Sci. Technol.*, 2022, vol. 97, pp. 229–38. https://doi.org/10.1016/j.jmst.2021.05.015.
27. H.T. He, J.X. Fang, J.X. Wang, T. Sun, Z. Yang, B. Ma, *et al.*: *Int. J. Refract. Met. Hard Mater.*, 2023, vol. 11, p. 116. https://doi.org/10.1016/j.ijrmhm.2023.106349.
28. S. Wu, D. Qiao, H. Zhao, J. Wang, and Y. Lu: *J. Alloys Compd.*, 2022, vol. 1, p. 889. https://doi.org/10.1016/j.jallcom.2021.161800.
29. J. Xu, R. Duan, K. Feng, C. Zhang, Q. Zhou, P. Liu, *et al.*: *Addit. Manuf. Lett.*, 2022, vol. 12, p. 3. https://doi.org/10.1016/j.addlet.2022.100079.
30. K. Zhou, Z. Wang, F. He, S. Liu, J. Li, J. Kai, *et al.*: *Addit. Manuf.*, 2020, vol. 10, p. 35. https://doi.org/10.1016/j.addma.2020.101410.
31. F. Haftlang and H.S. Kim: *A Perspective on Precipitation-Hardening High-Entropy Alloys Fabricated by Additive Manufacturing*, Elsevier, Amsterdam, 2021.
32. L.A.U. Farquhar: *Development of Refractory High Entropy Alloys for Additive Manufacturing*, University of Sheffield, Sheffield, 2024.
33. F. Bachmann, R. Hielscher, and H. Schaeben: in: *Solid State Phenomena*, vol. 160, Trans Tech Publications Ltd., 2010, pp. 63–68.
34. C.L.A. Leung, S. Marussi, M. Towrie, and R.C. Atwood: *Acta Mater.*, 2019, vol. 166, pp. 294–305. https://doi.org/10.1016/j.actamat.2018.12.027.
35. X. Yang, F. Gao, F. Tang, X. Hao, and Z. Li: *Metall. Mater. Trans. A Phys. Metall. Mater. Sci.*, 2021, vol. 52(10), pp. 4518–32. https://doi.org/10.1007/s11661-021-06405-3.
36. D. Gu and D. Dai: *J. Appl. Phys.*, 2016, vol. 120(8), 083104. https://doi.org/10.1063/1.4961410.
37. N.R. Philips, M. Carl, and N.J. Cunningham: *Metall. Mater. Trans. A*, 2020, vol. 51A, pp. 3299–3310. https://doi.org/10.1007/s11661-020-05803-3.
38. X. Wang, L.N. Carter, B. Pang, M.M. Attallah, and M.H. Loretto: *Acta Mater.*, 2017, vol. 4(128), pp. 87–95. https://doi.org/10.1016/j.actamat.2017.02.007.
39. A. DesprÃ©s, C. Mayer, M. Veron, E.F. Rauch, M. Bugnet, J.J. Blandin, *et al.*: *Materialia.*, 2021, https://doi.org/10.1016/j.mtla.2021.101037.
40. E. Bain: *Trans AIME*, 1924, vol. 70, p. 25.
41. G. Grimvall and B. Magyari-Köpe, E.N.M. Ozolin, and K.A. Persson: *Rev. Mod. Phys.*, 2012, vol. 84(2), pp. 945–86. https://doi.org/10.1103/RevModPhys.84.945.
42. Z.G. Zhu, Q.B. Nguyen, F.L. Ng, X.H. An, X.Z. Liao, P.K. Liaw, *et al.*: *Scripta Mater.*, 2018, vol. 154, pp. 20–24. https://doi.org/10.1016/j.scriptamat.2018.05.015.
43. A.S. Wu, D.W. Brown, M. Kumar, G.F. Gallegos, and W.E. King: *Metall. Mater. Trans. A*, 2014, vol. 45A, pp. 6260–70. https://doi.org/10.1007/s11661-014-2549-x.
44. D.D. Gu, W. Meiners, K. Wissenbach, and R. Poprawe: *Int. Mater. Rev.*, 2012, vol. 57(3), pp. 133–64.
45. P. Mercelis and J.P. Kruth: *Rapid Prototyp. J.*, 2006, vol. 12(5), pp. 254–65. https://doi.org/10.1108/13552540610707013.
46. Z. Tong, X. Ren, J. Jiao, W. Zhou, Y. Ren, Y. Ye, *et al.*: *J. Alloys Compd.*, 2019, vol. 785, pp. 1144–59. https://doi.org/10.1016/j.jallcom.2019.01.213.
47. Q. Chao, S. Thomas, N. Birbilis, P. Cizek, P.D. Hodgson, and D. Fabijanic: *Mater. Sci. Eng. A*, 2021, vol. 7, p. 821. https://doi.org/10.1016/j.msea.2021.141611.
48. Z. Wang, H. Wu, Y. Wu, H. Huang, X. Zhu, Y. Zhang, *et al.*: *Mater. Today*, 2022, vol. 54, pp. 83–89. https://doi.org/10.1016/j.mattod.2022.02.006.
49. C.R. Weinberger, B.L. Boyce, and C.C. Battaile: *Int. Mater. Rev.*, 2013, vol. 58(5), pp. 296–314.